Nanoscale

COMMUNICATION

View Article Online
View Journal | View Issue

Cite this: *Nanoscale*, 2017, **9**, 11841

Received 17th May 2017,
Accepted 18th July 2017

DOI: 10.1039/c7nr03530f

rsc.li/nanoscale

Solution synthesis and phase control of inorganic perovskites for high-performance optoelectronic devices†

Jia Liang,[a] Caixing Wang,[a] Peiyang Zhao,[a] Zhipeng Lu,[a] Yue Ma,[a] Zhaoran Xu,[a] Yanrong Wang,[a] Hongfei Zhu,[a] Yi Hu,[a] Guoyin Zhu,[a] Lianbo Ma,[a] Tao Chen,[a] Zuoxiu Tie,[a] Jie Liu[a,b] and Zhong Jin *[a]

An efficient method to synthesize well-crystallized inorganic cesium lead halide perovskites ($CsPbX_3$, X = I or Br) with high yield and high reproducibility was proposed. Notably, the as-prepared $CsPbI_3$ in the yellow orthorhombic phase (y-$CsPbI_3$) can be easily converted to the black cubic perovskite phase $CsPbI_3$ (b-$CsPbI_3$) after thermal annealing. Furthermore, two-terminal photodetectors and all-inorganic perovskite solar cells based on b-$CsPbI_3$ were fabricated, exhibiting high performances.

Metal halide perovskites have attracted considerable attention due to their excellent optical absorption, good carrier mobility and broad chemical tunability.[1–7] In particular, organic–inorganic hybrid lead halide perovskites have been regarded as promising materials for optoelectronic applications, such as solar cells,[8–15] light emitting diodes[16–19] and photo-driven water splitting.[20,21] In the past few years, the rapid growth of power conversion efficiencies in perovskite solar cells resulted in an explosion of interest in this area.[8–15] Up to now, the majority of research focuses on organic–inorganic hybrid lead halide perovskites, such as methylammonium lead trihalides and formamidinium lead trihalides ($MAPbX_3$ and $FAPbX_3$, X = Cl, Br, I or mixed halogens). However, the hybrid perovskites usually show serious instability against moisture, heat and ultraviolet (UV) light. To avoid this problem, inorganic perovskites (such as $CsPbX_3$) have attracted rapidly increasing attention recently, owing to the comparable properties and higher stability.[22–40]

Until now, most of the previous reports on the synthesis of inorganic perovskites were focused on direct film deposition using solution spin-coating or vapor-phase co-evaporation.[22–28] The colloidal synthesis of inorganic perovskite nanocrystals has only been developed very recently.[29–40] It is necessary to develop novel synthesis approaches with a higher yield and to avoid rigorous reaction conditions, such as high vacuum, inert gas protection, *etc*. In particular, for the practical application in optoelectronic devices, the batch production and phase control of inorganic perovskite materials with high crystallinity are urgently required. In this report, we demonstrate a facile and scalable synthesis method to produce inorganic cesium lead halides ($CsPbX_3$, X = I or Br) with high yield and reproducibility. Notably, the as-prepared $CsPbI_3$ in the yellow orthorhombic phase (y-$CsPbI_3$) can be easily converted to the black cubic perovskite phase $CsPbI_3$ (b-$CsPbI_3$) after thermal annealing above the phase-transition temperature. Furthermore, two-terminal photodetectors and all-inorganic perovskite solar cells based on b-$CsPbI_3$ were fabricated, exhibiting high performances and long-term stability.

As shown in Fig. 1a, large-yield and high-crystallinity y-$CsPbI_3$ with the orthorhombic phase can be prepared *via* a facile hydrothermal process with lead acetate ($Pb(Ac)_2$), cesium acetate ($Cs(Ac)_2$) and hydroiodic acid (HI) as precursors (as detailed in the Experimental methods section†). The morphology of the as-obtained y-$CsPbI_3$ crystals obtained after the hydrothermal process was characterized by scanning electron microscopy (SEM), as shown in Fig. 1b, exhibiting a uniform shape of microrods with an average length of ~50 μm and a width of 7–10 μm. The crystallinity and purity of y-$CsPbI_3$ were evaluated by powder X-ray diffraction (XRD), as displayed in Fig. 1c, and all the identified XRD peaks could be indexed to the standard pattern of $CsPbI_3$ in the yellow orthorhombic phase (JCPDS card no. 18-0376). To identify the compositions of y-$CsPbI_3$, X-ray photoelectron spectroscopy (XPS) was performed (Fig. 1d–g). The energy bands of Cs, Pb and I can be clearly identified in the survey XPS spectrum (Fig. 1d). A small peak of C 1s originating from adventitious carbon was also observed and set to 284.6 eV. The binding energies of Cs $3d_{3/2}$, Cs $3d_{5/2}$, Pb $4f_{5/2}$, Pb $4f_{7/2}$, I $3d_{3/2}$ and I $3d_{5/2}$ bands were determined after calibration, as shown in Fig. 1e–g and Table S1,†

[a]*Key Laboratory of Mesoscopic Chemistry of MOE and Collaborative Innovation Center of Chemistry for Life Sciences, School of Chemistry and Chemical Engineering, Nanjing University, Nanjing, Jiangsu 210093, China. E-mail: zhongjin@nju.edu.cn*

[b]*Department of Chemistry, Duke University, Durham, North Carolina 27708, USA. E-mail: j.liu@duke.edu*

†Electronic supplementary information (ESI) available: Experimental methods, additional figures and tables. See DOI: 10.1039/c7nr03530f

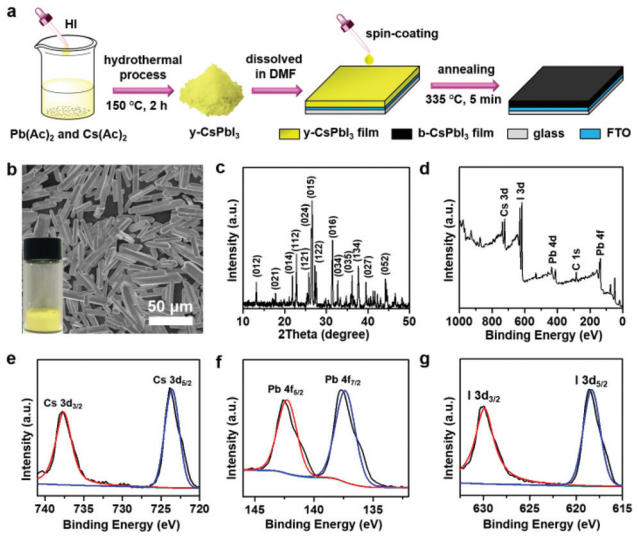

Fig. 1 (a) Schematic illustration of the solution-phase synthesis and thin film fabrication of $CsPbI_3$. (b) SEM image, (b) XRD pattern and (c) XPS survey of y-$CsPbI_3$. The inset in (b) shows a photograph of the as-prepared y-$CsPbI_3$ product obtained by the hydrothermal process. (e–g) Corresponding high-resolution XPS spectra of (e) Cs 3d, (f) Pb 4f and (g) I 3d regions of y-$CsPbI_3$.

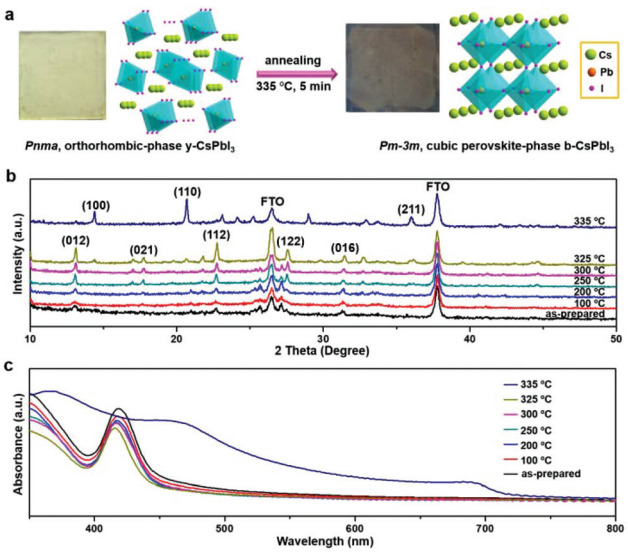

Fig. 2 (a) The change in film color and crystal structure from orthorhombic phase y-$CsPbI_3$ to cubic perovskite phase b-$CsPbI_3$ after annealing at 335 °C. (b) XRD patterns and (c) UV-vis absorbance spectra of $CsPbI_3$ films annealed at different temperatures. The XRD peaks marked with "FTO" in (b) are originating from the FTO substrate.

confirming the chemical compositions of y-$CsPbI_3$. Similarly, this synthetic strategy is also applicable for another cesium lead halide, $CsPbBr_3$, by replacing the hydroiodic acid precursor with hydrobromic acid. The SEM image and the XRD pattern of the as-prepared $CsPbBr_3$ are shown in Fig. S1a and b,† revealing its micro-polyhedral shape and crystalline structure in the monoclinic phase (JCPDS card no. 18-0364).

It is known that the crystal structure of $CsPbI_3$ can be orthorhombic, tetragonal or cubic polymorphs of the perovskite lattices, and the cubic perovskite phase is predominant at a high-temperature state.[29] The as-prepared y-$CsPbI_3$ obtained from hydrothermal synthesis in the orthorhombic (*Pnma*) space group exhibits a yellow color (as shown in the inset of Fig. 1b) and a distorted perovskite structure (Fig. 2a), in which the central lead atom is surrounded octahedrally by six iodine atoms with a tilted geometry in contrast to the orthogonal geometry of the ideal perovskite structure. To investigate the phase transition behavior of $CsPbI_3$ crystals, the y-$CsPbI_3$ product was dissolved in DMF, spin-coated on a fluorine-doped tin oxide (FTO) substrate, and then annealed at different temperatures. Fig. 2a shows that the color of the $CsPbI_3$ film changes from yellow to black after annealing at 335 °C, revealing that the phase transition temperature of $CsPbI_3$ from the yellow orthorhombic phase to the black cubic perovskite phase is around 335 °C. This phase change can also be distinguished by the change of XRD peaks at different temperatures, as shown in Fig. 2b. Fig. 2b shows that the XRD peak intensities of y-$CsPbI_3$ increase as the annealing temperature increases. This indicates that the crystallinity of the sample becomes higher along with the increase in annealing temperature, as indicated by the SEM images (Fig. S2†). After annealing at 335 °C for 1–2 min, the crystal structure of the $CsPbI_3$ sample changed to b-$CsPbI_3$ in the cubic perovskite (*Pm3m*) space group, exhibiting a three-dimensional framework of corner-connected PbI_6 octahedra with Cs cations located between the octahedra (Fig. 2a). The optical absorbance spectra of the annealed $CsPbI_3$ films were recorded using UV-vis spectroscopy, as shown in Fig. 2c. All the $CsPbI_3$ films annealed below 335 °C show similar absorbance spectra, owing to their unchanged orthorhombic phase. A closer observation reveals that the absorption edge of y-$CsPbI_3$ annealed below 335 °C shows a blue shift along with the increase in annealing temperature, and the color changes from yellow to light yellow (Fig. S3†). This may be ascribed to the improved crystallinity and the enlarged crystal size of y-$CsPbI_3$ after annealing, as evidenced by Fig. S2.† It should be noted that the color of y-$CsPbI_3$ films annealed at 330 °C for more than 3 min can also be changed to black; however, it will turn back to yellow immediately when the temperature is decreased to below 330 °C. The onset absorption wavelength of the as-prepared y-$CsPbI_3$ is around 450 nm (corresponding to 2.76 eV), which is too short to strongly absorb visible light. In contrast, the onset absorption wavelength of b-$CsPbI_3$ after phase transition is around 715 nm (corresponding to ~1.73 V), indicating that it is a promising material for optoelectronic devices. For the as-obtained $CsPbBr_3$, it exhibits an onset absorption wavelength of 540 nm, as shown in Fig. S1c,† which is also smaller than that of b-$CsPbI_3$.

To investigate the potential of inorganic perovskite $CsPbI_3$ for optoelectronic devices, two-terminal photodetectors based on both y-$CsPbI_3$ and b-$CsPbI_3$ were fabricated and tested. The insets in Fig. 3a and b show the schematic configuration of

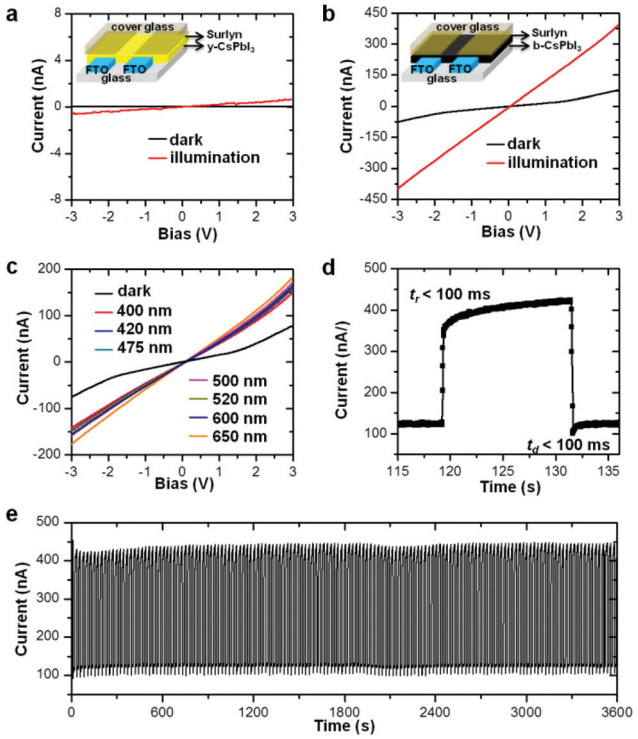

Fig. 3 Typical *I–V* ramp characteristics of (a) y-$CsPbI_3$- and (b) b-$CsPbI_3$-based photodetectors under darkness and simulated AM 1.5G illumination (100 mW cm^{-2}), respectively. The insets in (a) and (b) are the schematic configurations of the photodetectors based on y-$CsPbI_3$ and b-$CsPbI_3$, respectively. (c) *I–V* ramp characteristics of b-$CsPbI_3$ photodetectors under darkness and monochromatic light illumination with different wavelengths, respectively (the intensities of the lights of 400, 420, 475, 500, 520, 600 and 650 nm are 12, 10, 17, 13, 10, 14 and 17 mW cm^{-2}, respectively). (d) Typical photocurrent rise and decay curve magnified from (e). (e) Time-resolved photoresponse of b-$CsPbI_3$ photodetector at a bias of 3.0 V under simulated AM 1.5G illumination.

the device architectures used in this study. To prevent the influence of the ambient environment, the photodetectors were encapsulated by using cover glass and a hot-melt spacer (Surlyn 1702, 30 μm thick, Solaronix), as shown in the insets of Fig. 3a and b. The functional mechanism of the photodetectors is depicted in Fig. S4.† Under light illumination, the inorganic perovskite $CsPbI_3$ can absorb light and generate electron–hole pairs. Subsequently, the electron–hole pairs are rapidly separated and gathered by the electrodes under the applied electric field, therefore the device current is greatly increased in response to the light. Fig. 3a and b display the current–voltage (*I–V*) plots of y-$CsPbI_3$- and b-$CsPbI_3$-based photodetectors obtained under darkness and simulated solar illumination, respectively. The linear curves indicate that both y-$CsPbI_3$ and b-$CsPbI_3$ have good ohmic contacts with FTO electrodes, which are favorable for charge transfer. Owing to the wide bandgap of y-$CsPbI_3$ (2.76 eV), the y-$CsPbI_3$ photodetectors exhibit a weak response under light illumination. Under dark conduction, the b-$CsPbI_3$ photodetectors present a low current value, because of their intrinsic semiconductive properties, while under light illumination, the b-$CsPbI_3$ photodetectors show a much higher current density. The significant photocurrent density increase of b-$CsPbI_3$ photodetectors can be ascribed to the remarkable light harvesting capability resulting from the strong absorption in the visible spectrum region (Fig. 2c). Besides, the photoresponse performances of the b-$CsPbI_3$ photodetectors under illumination of different wavelengths were also measured, as shown in Fig. 3c, indicating that the b-$CsPbI_3$ photodetectors can work effectively under a broad wavelength range, which is superior to the previously reported $CsPbBr_3$-based photodetectors.[40] The photocurrent–time (*I–t*) response of the b-$CsPbI_3$ photodetector was measured at a bias of 3.0 V under intermittent light illumination with an on/off interval of 12 s (Fig. 3d and e), exhibiting the good reversibility and repeatability of b-$CsPbI_3$ photodetectors. It is well known that the rise time (t_r) and the delay time (t_d) are important parameters to evaluate the performance of a photodetector. Quantitatively, the t_r is defined as the time required for dark current to increase to 90% of the maximum value of the photocurrent density, or *vice versa*. As shown in Fig. 3d, both the t_r and t_d of the b-$CsPbI_3$ photodetector are less than 100 ms. This photoresponse rate is comparable to those of the previously-reported photodetectors based on ZnO nanoparticles, TiO_2 films, and other perovskite materials.[41–45] The strong light response of the b-$CsPbI_3$ photodetector can be ascribed to: (1) the good intrinsic light-harvesting capability of b-$CsPbI_3$, (2) the high quality of the b-$CsPbI_3$ film and (3) the good electric contact between b-$CsPbI_3$ and FTO electrodes with almost no interfacial barrier.

Recently, the design and preparation of novel inorganic halide perovskites have drawn tremendous attention because the performances of PSCs based on inorganic perovskites exhibited rapid progress over the past two years.[22–28] The b-$CsPbI_3$ product was also used for the fabrication of all-inorganic perovskite solar cells. Fig. 4a and b display the schematic cross-sectional view of two kinds of b-$CsPbI_3$-based all-inorganic perovskite solar cells with the structures of FTO/compact TiO_2 (c-TiO_2)/mesoporous TiO_2 (m-TiO_2)/b-$CsPbI_3$/carbon (AIPSC-1) and FTO/c-TiO_2/b-$CsPbI_3$/carbon (AIPSC-2), respectively. All of the organic components in common organic–inorganic hybrid perovskite solar cells, such as organic–inorganic hybrid perovskites (usually $MAPbI_3$ or $FAPbI_3$), organic hole transport materials (usually 2,2′,7,7′-tetrakis(*N*,*N*′-di-*p*-methoxyphenylamine)-9,9′-spirobifluorene or polytriarylamine), and organic additives in hole transport materials (mainly lithium bis(trifluoromethanesulfonyl)imide or *tert*-butylpyridine), were completely eliminated from the all-inorganic perovskite solar cells, to prevent the disadvantages caused by the organic components, especially the high cost and the performance instability against high temperature, moisture, *etc*. Fig. 4c exhibits the energy band levels of all-inorganic perovskite solar cells, revealing the electron extraction from the b-$CsPbI_3$ conduction band to the TiO_2 conduction band and the hole extraction from the $CsPbI_3$ valence band to the carbon electrode.[10,11,22,46] In this configuration, a layer of the carbon electrode works as a bifunctional film for both effective hole extraction and collection since it has a suitable

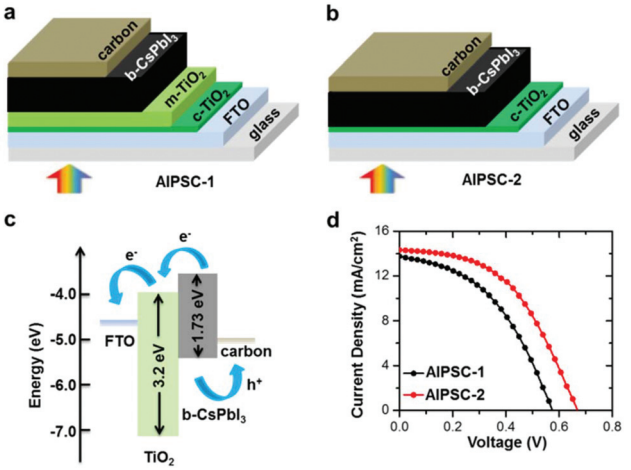

Fig. 4 Schematic cross-sectional view of the solar cells with structures of (a) FTO/c-TiO_2/m-TiO_2/b-$CsPbI_3$/carbon (labeled as AIPSC-1) and (b) FTO/c-TiO_2/b-$CsPbI_3$/carbon (labeled as AIPSC-2), respectively. (c) Energy band diagram of the b-$CsPbI_3$ based all-inorganic perovskite solar cells, showing the electron injection and hole extraction routes. (d) *J–V* plots of the AIPSC-1 and AIPSC-2 under simulated solar AM 1.5G illumination.

work function (−5.0 eV);[10] therefore, both organic hole transport materials and noble metal electrodes can be replaced by the carbon electrode with remarkable stability, good processability and low cost. The photocurrent density–voltage (*J–V*) plots of AIPSC-1 and AIPSC-2 under simulated solar AM 1.5G illumination are shown in Fig. 4d, and the corresponding performance parameters are listed in Table S2.† The AIPSC-1 with a m-TiO_2 layer exhibits a power conversion efficiency (PCE) of 3.48% with a short-circuit density (J_{SC}) of 13.74 mA cm^{-2}, an open-circuit voltage (V_{OC}) of 0.58 V, and a fill factor (FF) of 0.44. In contrast, the all-inorganic perovskite solar cells without the m-TiO_2 layer present an increase in all the performance parameters. As shown in Fig. 4d and Table S2,† the AIPSC-2 shows a higher PCE of 4.65% with a J_{SC} of 14.31 mA cm^{-2}, a V_{OC} of 0.67 V and a FF of 0.48. These results indicate that the b-$CsPbI_3$ film has sufficient carrier diffusion length, therefore it is not necessary to introduce the m-TiO_2 layer to extract electrons from $CsPbI_3$. To the best of our knowledge, the PCE value of $CsPbI_3$/carbon-based AIPSC-2 is higher than those of the previously reported $CsPbI_3$/spiro-OMeTAD/metal (Au or Ag)-based perovskite solar cells.[24,25] Moreover, the facile synthesis method of b-$CsPbI_3$ in this work provides a scalable approach to prepare all-inorganic perovskite solar cells with an easy fabrication process. In theory, with a bandgap of 1.73 eV, the maximum J_{SC} of $CsPbI_3$-based all-inorganic PSCs can reach ~21 mA cm^{-2} under AM 1.5G illumination. Therefore, there is still plenty of room for us to further improve the performances of $CsPbI_3$-based all-inorganic PSCs in the future.

In summary, we have developed a batch-sale solution-phase synthesis method for the preparation of inorganic cesium lead halides ($CsPbX_3$, X = I or Br) with high yield and good quality. The as-prepared y-$CsPbI_3$ in the orthorhombic phase can be easily converted to b-$CsPbI_3$ in the cubic perovskite phase after thermal annealing. The photodetectors based on b-$CsPbI_3$ show a remarkable performance under a broad wavelength range of light illumination, owing to the appropriate bandgap and strong optical absorption. Moreover, all-inorganic perovskite solar cells based on b-$CsPbI_3$ and carbon electrode were also fabricated, which avoided the disadvantages of organic components in common organic–inorganic hybrid perovskite solar cells, such as high-cost and instability against heat and humidity. We expect that the synthetic method reported here can be extended to the synthesis of other inorganic perovskite materials, such as Sn-based perovskites with less toxic elements, contributing to the batch fabrication of high-performance and low-cost perovskite devices.

Acknowledgements

This work is supported by the National Key Research and Development Program of China (2017YFA0208200, 2016YFB0700600), the National Key Basic Research Program (2015CB659300), the Projects of NSFC (21403105, 21573108), the China Postdoctoral Science Foundation (2015M581775, 2015M580412 and 2015M581769), the Natural Science Foundation of Jiangsu Province for Young Scholars (BK20150583, BK20160647), the Fundamental Research Funds for the Central Universities (020514380107), and a project funded by the Priority Academic Program Development of Jiangsu Higher Education Institutions.

Notes and references

1 S. D. Stranks, G. E. Eperon, G. Grancini, C. Menelaou, M. J. P. Alcocer, T. Leijtens, L. M. Herz, A. Petrozza and H. J. Snaith, *Science*, 2013, **342**, 341–344.
2 G. Xing, N. Mathews, S. Sun, S. S. Lim, Y. M. Lam, M. Graetzel, S. Mhaisalkar and T. C. Sum, *Science*, 2013, **342**, 344–347.
3 D. Shi, V. Adinolfi, R. Comin, M. Yuan, E. Alarousu, A. Buin, Y. Chen, S. Hoogland, A. Rothenberger, K. Katsiev, Y. Losovyj, X. Zhang, P. A. Dowben, O. F. Mohammed, E. H. Sargent and O. M. Bakr, *Science*, 2015, **347**, 519–522.
4 Q. Dong, Y. Fang, Y. Shao, P. Mulligan, J. Qiu, L. Cao and J. Huang, *Science*, 2015, **347**, 967–970.
5 D. W. deQuilettes, S. M. Vorpahl, S. D. Stranks, H. Nagaoka, G. E. Eperon, M. E. Ziffer, H. J. Snaith and D. S. Ginger, *Science*, 2015, **348**, 683–686.
6 G. Grancini, A. R. S. Kandada, J. M. Frost, A. J. Barker, M. De Bastiani, M. Gandini, S. Marras, G. Lanzani, A. Walsh and A. Petrozza, *Nat. Photonics*, 2015, **9**, 695–701.
7 N. S. Makarov, S. Guo, O. Isaienko, W. Liu, I. Robel and V. I. Klimov, *Nano Lett.*, 2016, **16**, 2349–2362.
8 J. Burschka, N. Pellet, S.-J. Moon, R. Humphry-Baker, P. Gao, M. K. Nazeeruddin and M. Graetzel, *Nature*, 2013, **499**, 316–319.

9 M. Liu, M. B. Johnston and H. J. Snaith, *Nature*, 2013, **501**, 395–398.
10 A. Mei, X. Li, L. Liu, Z. Ku, T. Liu, Y. Rong, M. Xu, M. Hu, J. Chen, Y. Yang, M. Graetzel and H. Han, *Science*, 2014, **345**, 295–298.
11 W. S. Yang, J. H. Noh, N. J. Jeon, Y. C. Kim, S. Ryu, J. Seo and S. I. Seok, *Science*, 2015, **348**, 1234–1237.
12 W. Chen, Y. Wu, Y. Yue, J. Liu, W. Zhang, X. Yang, H. Chen, E. Bi, I. Ashraful, M. Graetzel and L. Han, *Science*, 2015, **350**, 944–948.
13 D. P. McMeekin, G. Sadoughi, W. Rehman, G. E. Eperon, M. Saliba, M. T. Hoerantner, A. Haghighirad, N. Sakai, L. Korte, B. Rech, M. B. Johnston, L. M. Herz and H. J. Snaith, *Science*, 2016, **351**, 151–155.
14 P. Cui, D. Wei, J. Ji, D. D. Song, Y. Y. Li, X. Liu, J. Huang, T. Y. Wang, J. B. You and M. C. Li, *Solar RRL*, 2017, **1**, 1600027.
15 Y. Hu, S. Si, A. Mei, Y. Rong, H. Liu, X. Li and H. Han, *Solar RRL*, 2017, **1**, 1600019.
16 H. Cho, S.-H. Jeong, M.-H. Park, Y.-H. Kim, C. Wolf, C.-L. Lee, J. H. Heo, A. Sadhanala, N. Myoung, S. Yoo, S. H. Im, R. H. Friend and T.-W. Lee, *Science*, 2015, **350**, 1222–1225.
17 X. Y. Chin, D. Cortecchia, J. Yin, A. Bruno and C. Soci, *Nat. Commun.*, 2015, **6**, 7383.
18 Y.-H. Kim, H. Cho, J. H. Heo, T.-S. Kim, N. Myoung, C.-L. Lee, S. H. Im and T.-W. Lee, *Adv. Mater.*, 2015, **27**, 1248–1254.
19 H. Zhang, H. Lin, C. Liang, H. Liu, J. Liang, Y. Zhao, W. Zhang, M. Sun, W. Xiao, H. Li, S. Polizzi, D. Li, F. Zhang, Z. He and W. C. H. Choy, *Adv. Funct. Mater.*, 2015, **25**, 7226–7232.
20 J. Luo, J.-H. Im, M. T. Mayer, M. Schreier, M. K. Nazeeruddin, N.-G. Park, S. D. Tilley, H. J. Fan and M. Graetzel, *Science*, 2014, **345**, 1593–1596.
21 Gurudayal, D. Sabba, M. H. Kumar, L. H. Wong, J. Barber, M. Graetzel and N. Mathews, *Nano Lett.*, 2015, **15**, 3833–3839.
22 J. Liang, C. Wang, Y. Wang, Z. Xu, Z. Lu, Y. Ma, H. Zhu, Y. Hu, C. Xiao, X. Yi, G. Zhu, H. Lv, L. Ma, T. Chen, Z. Tie, Z. Jin and J. Liu, *J. Am. Chem. Soc.*, 2016, **138**, 15829–15832.
23 J. Liang, C. Wang, Y. Wang, Z. Xu, Z. Lu, Y. Ma, H. Zhu, Y. Hu, C. Xiao, X. Yi, G. Zhu, H. Lv, L. Ma, T. Chen, Z. Tie, Z. Jin and J. Liu, *J. Am. Chem. Soc.*, 2017, **139**, 2852–2852.
24 G. E. Eperon, G. M. Paterno, R. J. Sutton, A. Zampetti, A. A. Haghighirad, F. Cacialli and H. J. Snaith, *J. Mater. Chem. A*, 2015, **3**, 19688–19695.
25 P. Luo, W. Xia, S. Zhou, L. Sun, J. Cheng, C. Xu and Y. Lu, *J. Phys. Chem. Lett.*, 2016, **7**, 3603–3608.
26 M. Kulbak, D. Cahen and G. Hodes, *J. Phys. Chem. Lett.*, 2015, **6**, 2452–2456.
27 M. Kulbak, S. Gupta, N. Kedem, I. Levine, T. Bendikov, G. Hodes and D. Cahen, *J. Phys. Chem. Lett.*, 2016, **7**, 167–172.
28 A. Swarnkar, A. R. Marshall, E. M. Sanehira, B. D. Chernomordik, D. T. Moore, J. A. Christians, T. Chakrabarti and J. M. Luther, *Science*, 2016, **354**, 92–95.
29 L. Protesescu, S. Yakunin, M. I. Bodnarchuk, F. Krieg, R. Caputo, C. H. Hendon, R. X. Yang, A. Walsh and M. V. Kovalenko, *Nano Lett.*, 2015, **15**, 3692–3696.
30 I. Lignos, S. Stavrakis, G. Nedelcu, L. Protesescu, A. J. deMello and M. V. Kovalenko, *Nano Lett.*, 2016, **16**, 1869–1877.
31 Y. Bekenstein, B. A. Koscher, S. W. Eaton, P. Yang and A. P. Alivisatos, *J. Am. Chem. Soc.*, 2015, **137**, 16008–16011.
32 D. Zhang, S. W. Eaton, Y. Yu, L. Dou and P. Yang, *J. Am. Chem. Soc.*, 2015, **137**, 9230–9233.
33 Y. Wang, X. Li, J. Song, L. Xiao, H. Zeng and H. Sun, *Adv. Mater.*, 2015, **27**, 7101–7108.
34 J. Song, J. Li, X. Li, L. Xu, Y. Dong and H. Zeng, *Adv. Mater.*, 2015, **27**, 7162–7167.
35 Y. Wang, X. Li, X. Zhao, L. Xiao, H. Zeng and H. Sun, *Nano Lett.*, 2016, **16**, 448–453.
36 S. Sun, D. Yuan, Y. Xu, A. Wang and Z. Deng, *ACS Nano*, 2016, **10**, 3648–3657.
37 X. Li, Y. Wu, S. Zhang, B. Cai, Y. Gu, J. Song and H. Zeng, *Adv. Funct. Mater.*, 2016, **26**, 2435–2445.
38 X. Zhang, H. Lin, H. Huang, C. Reckmeier, Y. Zhang, W. C. H. Choy and A. L. Rogach, *Nano Lett.*, 2016, **16**, 1415–1420.
39 M. Lai, Q. Kong, C. G. Bischak, Y. Yu, L. Dou, S. W. Eaton, N. S. Ginsberg and P. Yang, *Nano Res.*, 2017, **10**, 1107–1114.
40 D. Zhang, Y. Yang, Y. Bekenstin, Y. Yu, N. A. Gibson, A. B. Wong, S. W. Eaton, N. Korienko, Q. Kong, M. Lai, A. P. Alivisatos, S. R. Leone and P. Yang, *J. Am. Chem. Soc.*, 2016, **138**, 7236–7239.
41 Z. Wang, H. Wang, B. Liu, W. Qiu, J. Zhang, S. Ran, H. Huang, J. Xu, H. Han, D. Chen and G. Shen, *ACS Nano*, 2011, **5**, 8412–8419.
42 K. Liu, M. Sakurai, M. Liao and M. Aono, *J. Phys. Chem. C*, 2010, **114**, 19835–19839.
43 P. Zhu, S. Gu, X. Shen, N. Xu, Y. Tan, S. Zhuang, Y. Deng, Z. Lu, Z. Wang and J. Zhu, *Nano Lett.*, 2016, **16**, 871–876.
44 X. Hu, X. Zhang, L. Liang, J. Bao, S. Li, W. Yang and Y. Xie, *Adv. Funct. Mater.*, 2014, **24**, 7373–7380.
45 H. Lu, W. Tian, F. Cao, Y. Ma, B. Gu and L. Li, *Adv. Funct. Mater.*, 2016, **26**, 1296–1302.
46 G. Li, F. W. R. Rivarola, N. J. L. K. Davis, S. Bai, T. C. Jellicoe, F. de la Pena, S. Hou, C. Ducati, F. Gao, R. H. Friend, N. C. Greenham and Z.-K. Tan, *Adv. Mater.*, 2016, **28**, 3528–3534.